CITATION

Lehner, S., A. Pleskachevsky, D. Velotto, and S. Jacobsen. 2013. Meteo-marine parameters and their variability observed by high resolution satellite radar images. Oceanography 26(2):80–91, http://dx.doi.org/10.5670/oceanog.2013.36.

DOI

http://dx.doi.org/10.5670/oceanog.2013.36

Meteo-Marine Parameters and Their Variability

Observed by High-Resolution Satellite Radar Images

BY SUSANNE LEHNER, ANDREY PLESKACHEVSKY, DOMENICO VELOTTO, AND SVEN JACOBSEN

TerraSAR-X ScanSAR Wide image acquired over the German Bight on March 29, 2013, at 17:11 UTC. It covers an area of 400 km × 250 km with 38 m resolution.

ABSTRACT. New radar satellites image the sea surface with resolutions as high as 1 m. A large spectrum of ocean processes can be estimated using such Earth observation data. These data have been applied to investigations of geophysical processes as well as to forecast model validations and near-real-time services. The numerous processes, parameters, and features observed in high-resolution synthetic aperture radar images include winds, waves (with wavelengths as small as 30 m), oil slicks, waterline changes, changes in seabed morphology in shallow waters, wakes and bow waves of ships, underwater topography, wave energy flux along wave tracks from deep water to the coast, and breaking waves. New algorithms have been developed that are capable of taking into account fine-scale effects in coastal areas.

NEW SAR MISSIONS FOR OCEANOGRAPHIC APPLICATIONS

Knowledge of marine and meteorological parameters is important for operational oceanographic services. In situ measurements and global, regional, and fine-resolution forecast models provide information on wind, sea state, and related processes. Spaceborne sensors are especially useful because of their global coverage and their independence from additional input data as compared to in situ methods and mathematical simulations. Remote-sensing data, in particular those acquired from spaceborne synthetic aperture radar (SAR), are an unparalleled source for model validation and verification in the open sea and in coastal zones because these data can also be collected independent of sunlight and cloud coverage.

Spaceborne SAR is a unique sensor that provides two-dimensional information about the ocean surface. The latest-generation of high-resolution SARs is particularly suitable for many ocean and coastal applications. In the last few years, a number of high-resolution X-band radar satellites have been launched, for example, TerraSAR-X, TanDEM-X, and COSMO-SkyMed.

Their data provide new perspectives on sea state and related processes in coastal areas, where sea surface variability plays a significant role. A wide range of features and signatures can be observed in these data, including surface winds and gusts, individual waves and their refraction, and effects of breaking waves. Knowledge of such background geophysical processes and an understanding of how they are imaged by SAR are important to successful SAR data processing and use of the results in terms of safety and security issues. Figure 1 shows an example of the effect of improved resolution on imaging coastal features such as breaking waves.

The X-band TerraSAR-X satellite was launched in June 2007 (http://www.dlr.de/TerraSAR-X) and its twin, TanDEM-X, in June 2010. TerraSAR-X and TanDEM-X operate from an altitude of 514 km in sun-synchronous orbits, with ground speeds of 7 km s^{-1} (15 orbits per day). The two satellites orbit in close formation with typical distances between them of 250 to 500 m. They operate with a wavelength of 31 mm and frequency of 9.6 GHz. The repeat cycle is 11 days, but the same region can be imaged with different incidence angles after three days, depending on image latitude.

Typical incidence angles range between 20° and 55°. Coverage and resolution depend on satellite mode: stripmap covers 30 km × 50 km with a resolution of about 3 m, while spotlight covers 10 km × 10 km with resolution of about 1 m (Breit et al., 2010).

As is known, targets that are moving to the SAR sensor will not be imaged in their real positions; they are shifted in flight direction. This Doppler effect, also called "train off the rails," plays a special role in the SAR imaging of moving waves. Compared to earlier SAR missions like Envisat Advanced SAR (ASAR), TerraSAR-X offers a number of advantages in addition to its higher resolution. In particular, the Doppler shift of scatterers, moving with velocity u_r toward the sensor (radial velocity) at distance R_o (slant range) is reduced. For example, for the same incidence angle of 22° and $u_r = 1$ m s^{-1}, the target's displacement in azimuth direction $D_x = (u_r / V_{sar}) \cdot R_o$ (Lyzenga et al., 1985) is ~ 73 m for TerraSAR-X but almost twice as large, ~ 115 m, for Envisat due to different platform velocity V_{sar} and slant range R_o (Envisat altitude was 800 km). Thus, the smoothing of moving wave crests (also called the bunching effect; Alpers and Rufenach, 1979) is noticeably reduced. As a result, imaging of the ocean surface is more stable, and the shortest waves imaged have wavelengths of ~ 25 to 30 m.

Susanne Lehner (*susanne.lehner@dlr.de*), **Andrey Pleskachevsky, Domenico Velotto**, *and* **Sven Jacobsen** *are all on the staff of the German Aerospace Center (DLR), Remote Sensing Technology Institute, Bremen, Germany.*

PROCESSES AND FEATURES OBSERVED IN SAR HIGH-RESOLUTION IMAGES

Knowledge of basic geophysical processes and what remote-sensing mechanism was used to collect the data is necessary for successful processing of images and for use in near-real-time services. The images contain information on wind and on sea state-related processes that must be properly extracted and assessed.

Morphodynamic Developments in Coastal Areas

Changes in seabed morphology in shallow waters can be mapped using SAR images. Wave action in coastal areas, where storms can change the soft seabed relatively rapidly, plays a key role in erosion and transformation of the seabed and the shoreline. For example, in Figure 2, a TerraSAR-X stripmap scene acquired at low tide over Elbe Estuary in the North Sea on November 11, 2008, showing sandbanks that have been partially eroded and split near tidal inlets is compared with smoother bathymetry in the same area processed by BAW (German Federal Waterways Engineering and Research Institute) in 2006. These bathymetry changes can be observed in the SAR image as a result of the way waves propagate and disperse in the estuary, as well as in the flow of local currents.

Sea State: Individual Long Wave Refraction and Underwater Topography

In coastal areas, underwater topography influences the refraction of long-period swells at water depths shallower than 70 to 50 m. Ocean surface wave properties change when water depths become less than about half of their wavelength. When a long-period ocean swell propagates toward shore, its wavelength shortens and its wave height increases due to conservation of energy.

The algorithm used to obtain swell wavelength and direction from TerraSAR-X images is based on FFT (Fast Fourier Transform) analysis of subscenes with dimensions of 800 m × 800 m. By computing the FFT for the selected subimage, a two-dimensional image spectrum in wave number space is retrieved. The peak in the two-dimensional spectrum determines peak wavelength and peak wave direction of all waves in the subimage. The retrieved wave directions have an ambiguity of 180° due to the static nature of a SAR image. In coastal areas where wave shoaling and refraction are recognized, propagation direction toward the coast is unambiguous. Starting in the open sea, the box for the FFT is moved along with the wave, and a new FFT is computed. This procedure is repeated until the corners of the FFT box reach the shoreline. In this way, a wave can be tracked from the open sea to the shoreline, and changes in its wavelength and direction can be measured. Wind streaks and ocean wind patterns are removed from the spectra by filtering for analyzed wavelengths between about 50 m and 300 m (background values must be checked for every scene). The
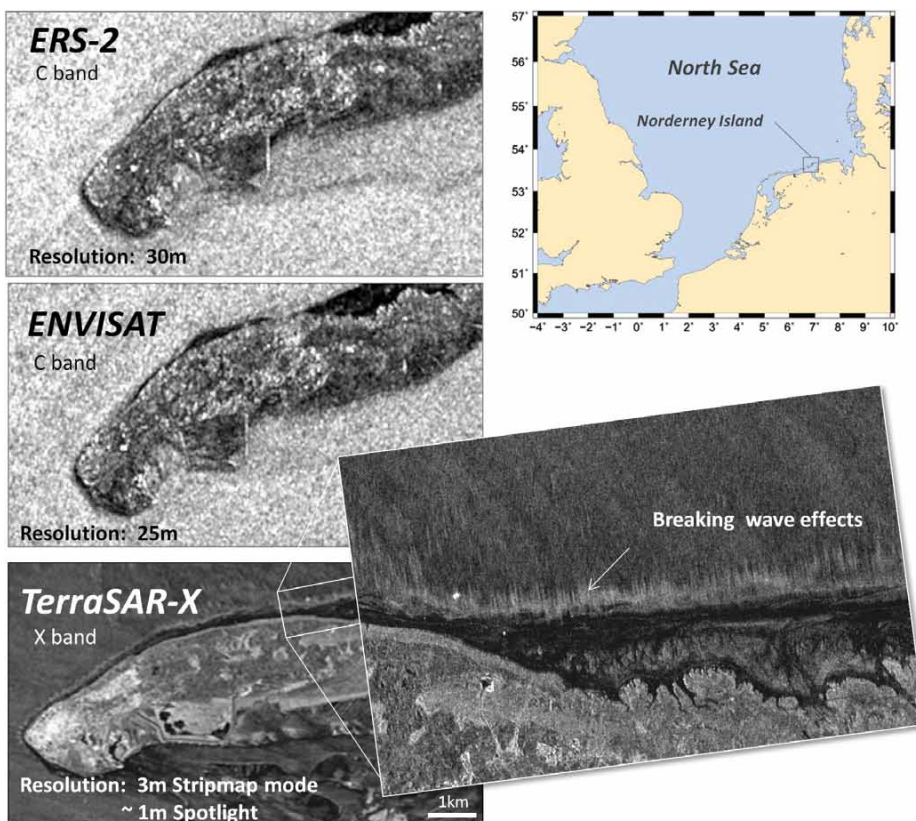

Figure 1. Effect of the improved resolution of the new synthetic aperture radar (SAR) satellites. Details of images from ERS-2 (1995–2011), Envisat ASAR (2002–2012), and TerraSAR-X (launched in 2007) acquired over Norderney Island in the North Sea.

translation of the FFT box to the next point in the swell propagation direction varies in range by ± 15° in order to avoid switching to another wave system in the case of cross seas.

Figure 3 (left) shows a TerraSAR-X spotlight image acquired over Rottenest Island, Australia, on October 20, 2009, with one wave ray. The island is situated ~ 50 km off the coast of Perth, Western Australia (115°30'E, 32°00'S). The long-swell waves induced in the Indian Ocean (storm peak about 1,500 km southwest of the area three days before) and propagating toward the island are visible in the image, and the refraction is well pronounced. This SAR image was special ordered so that long waves could be acquired for bathymetry estimation. The wave

forecast by the US National Oceanic and Atmospheric Administration (NOAA) WAVEWATCH III model (http://polar.ncep.noaa.gov/waves) was used to determine the appropriate acquisition time, and it was applied one week before the TerraSAR-X image acquisition. Figure 3 (middle) shows the TerraSAR-X image with 40 wave rays identified. Using 200 wave rays, the wavelength field was obtained for a uniform grid of 150 m resolution. The depths d (Figure 3, right) were derived using the dispersion relation:

$$d(L_p, \omega_p) = \frac{L_p}{2\pi} \, \text{atanh} \, \frac{\omega_p^2 L_p}{2\pi g}, \qquad (1)$$

where g is gravitational acceleration and ω_p is the angular wave peak frequency ($\omega_p = 2\pi / T_p$; T_p is the peak period). The peak period needed in

equation 1 is obtained using a combination of first guess and analysis of the tracks (T_p = 13.25 sec). The longest observed wave in the image is L_{max} = 245 m, and a threshold for minimal peak period for this wavelength is obtained from the deepwater relation $T_p \, min = (2\pi L_{max}/g)^{0.5}$ = 12.25 s.

The estimated underwater topography was compared to sonar measurements on the same grid. About 50% of the compared area had an error range of about ± 10% of the local depth. The obtained bathymetry has an accuracy on the order of 15% for depths of 60 to 20 m. Application of the SAR-based method described here is generally dependent on sea state (swell availability) and data acquisition quality. The latter is influenced
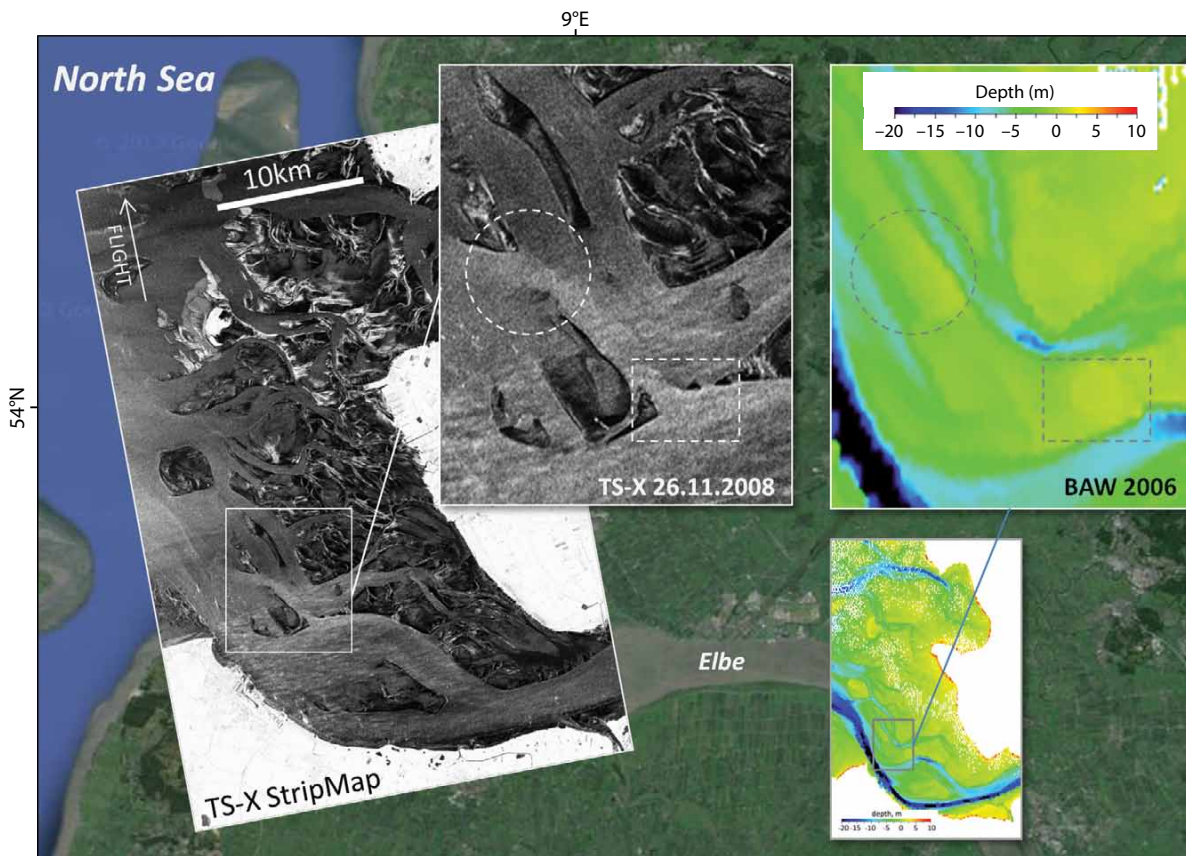

Figure 2. TerraSAR-X stripmap scene (left) with a coverage of 30 km × 50 km and resolution of 3 m, acquired over Elbe Estuary, German Bight, North Sea, on November 26, 2008, 17:10 UTC (low tide). The inset shows the change in Elbe Estuary bathymetry since 2006 when the BAW (German Federal Waterways Engineering and Research Institute) bathymetry map (right) was completed: a long bank was partially eroded and split by inlets (compare areas in dashed circles and squares). *Background image © Google Maps*

by artifacts, nonlinear SAR imaging effects (e.g., availability of local wind sea smearing in the image, breaking waves, ships with wakes), and the complexity of the topography itself (e.g., reef belts can destroy swell waves long before they reach the coast being investigated; Pleskachevsky et al., 2011). The method was successfully tested for different areas and sea states—the Duck Research Pier (North Carolina, USA, range traveling waves), Port Phillip (Melbourne, Australia, azimuth traveling waves), and around Helgoland Island (German Bight, North Sea) (Brusch et al., 2011).

To complete the bathymetric maps, QuickBird optical satellite data were used to map extreme shallow waters (< 10 m depth) near the coast. The algorithms for bathymetry estimation from optical and SAR data were combined and integrated in order to cover different depth domains. The two techniques make use of different physical phenomena and mathematical treatments. Optical methods are based on sunlight reflection analysis and provide depths up to 20 m in calm weather conditions. Depth estimation from SAR is based on the observation of long waves and covers water depths between 70 m and 10 m. Water depths from 20 m to 10 m are where synergy of data from both sources arises. This new technique provides a platform for coastal bathymetric mapping over a broad area on a scale that is relevant to marine planners, managers, and the offshore industry.

In addition to depth estimation, the SAR-based methodology allows detection of shoals such as underwater mountains, reefs, and sand bars with depths < 30 m, even if the quality of sea state information is insufficient for accurately obtaining bathymetry. The remotely sensed information on shoals (e.g., reefs) can be integrated into maritime ship safety and warning systems.

Surface Wind and Integrated Sea State Parameters

Synthetic aperture radar can provide wind information over the ocean by measuring sea surface roughness. A new algorithm XMOD-2 has been developed for TerraSAR-X data that takes the full nonlinear physical model function into account. At the same time, the corresponding sea state parameters can be estimated from the same image. A new empirical model function XWAVE-2 for obtaining significant wave height has been developed for X-band data. The algorithm is based on analysis of image spectra and uses parameters fitted with co-located buoy data and information
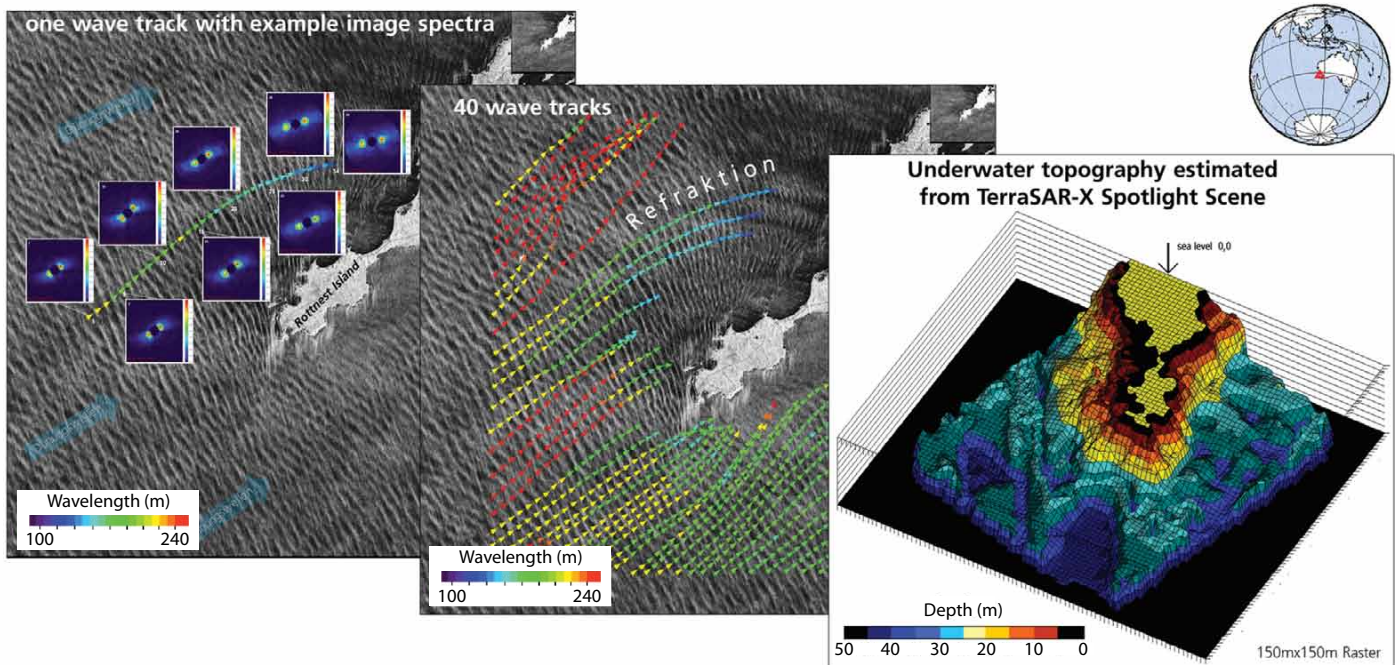

Figure 3. TerraSAR-X spotlight image (left) with dimensions of 10 km × 10 km and resolution of 1 m acquired over Rottenest Island, Australia, on October 20, 2009. (left) Normalized radar cross section (NRCS) and one wave track with example image spectra. (center) Forty wave rays (colored lines) tracked on the image. (right) Bathymetry (uniform raster, 150 m resolution) estimated from the TerraSAR-X image data. To complete the bathymetric maps in the shallowest areas (< 10 m water depth) near the coastline, optical data from the QuickBird satellite were used.

on spectra peak direction and incidence angle. The newly developed empirical algorithm estimates significant wave height H_s directly from TerraSAR-X image spectra without using a priori information and without temporal transferring into wave spectra.

Wind Estimation Algorithm XWAVE-2

The SAR wind field retrieval approach was first developed for C-band SAR provided by, for example, ERS-2 and Envisat ASAR. These approaches used empirically derived Geophysical Model Functions (GMF) that related local wind conditions and sensor geometry to radar cross-section values (e.g., CMOD4 or CMOD5). To utilize the new SAR systems, an X-band linear algorithm XMOD-1 and later a nonlinear XMOD-2 were established for VV- and HH-polarized data to obtain wind fields (Ren et al., 2012; Li and Lehner, in press). The relationship between X-band radar cross section and wind speed, wind direction, and incidence angle in XMOD-2 is given by:

$$\sigma_o(U,\theta,\varphi) = B_0^p(U_{10},\theta)(1 + B_1(U_{10},\theta)\cos(\varphi) + B_2(U_{10},\theta)\cos(2\varphi)), \quad (2)$$

where σ_o is the normalized radar cross section (NRCS), U is the wind speed, and φ is the relative wind direction. This is applicable for an incidence angle θ between 20° and 60° and wind speeds from 2 m s^{-1} to 25 m s^{-1}. The parameters $B_i\ i = 0,2$ are tuned using the measurement data sets. To determine wind direction, streak structures on the sea surface of the image are used. These are produced by airflow turbulent eddies at the boundary layer (Etling and Brown, 1993; Sikora and Ufermann, 2000). Shadows

behind the coast also provide evidence of wind blowing from the coast.

Data from the Spaceborne Imaging Radar-C/X (SIR-C/X) mission in 1994 and from the European Center for Medium-Range Weather Forecasts (ECMWF) reanalyzed wind fields ERA-40 (*ECMWF Re-A*nalysis of the global atmosphere and surface conditions for 45 years) were used to tune the algorithm. The results were validated using in situ measurements from co-located buoys and modeled data with different resolution (HIRLAM model and DWD COSMO). The wind field can be retrieved practically to 20 m resolution by the XMOD algorithm for TerraSAR-X images. In contrast to the previously developed XMOD-1, XMOD-2 consists of a set of nonlinear GMFs and thus depicts the difference between upwind and downwind of the sea surface backscatter in X-band SAR imagery. By exploiting 371 co-locations with in situ buoy measurements that are used as the tuning data set, together with analysis wind model results, the retrieved TerraSAR-X / TanDEM-X sea surface wind speed using XMOD-2 shows close agreement with buoy measurements with a bias of –0.32 m s^{-1}, a root mean square error (RMSE) of 1.44 m s^{-1}, and a scatter index (SI) of 16.0%. Further validation using an independent data set of 52 cases shows a bias of –0.17 m s^{-1}, an RMSE of 1.48 m s^{-1}, and an SI of 17.0% compared to buoy measurements (Li and Lehner, in press).

XWAVE-2 Empirical Algorithm to Derive Sea State Parameters

An empirical X-WAVE-1 model for obtaining integrated wave parameters has been developed for X-band data

(Bruck et al., 2011). The algorithm was based on analysis of image spectra and uses parameters fitted with co-located buoy data and information on spectra peak direction and incidence angle. The equation for the newly developed XWAVE-2 algorithm for deriving significant wave height directly from TerraSAR-X SAR image spectra is

$$H_s = a_1 \cdot \sqrt{(E \cdot \sin\theta)(1.0 + a_2\cos(\alpha))} + a_3, \quad (3)$$

where α is the wave peak direction related to the azimuth direction ($0° \leq \alpha \leq 90°$). The cosine function in the formula describes the dependence of wave peak direction in the image relative to satellite flight direction, and E is the integrated value of the directional wave number spectrum. Parameters a_1, a_2, and a_3 are the coefficients tuned to various data sets and are dependent on incidence angle θ. They are determined from a fit between E and the co-located significant wave height, computed by the DWD wave model, co-located buoy measurements, WaMoS-II (Wave Monitoring System), and radar altimeter data (Bruck and Lehner, 2010; Pontes et al., 2010). The peak period T_p corresponds to the wave period with maximum energy in the two-dimensional spectrum in the frequency domain. E is the integrated value of the image spectrum obtained by standard Fourier analysis done on a subscene of a radiometrically calibrated TerraSAR-X intensity image. The integration domain chosen is limited by minimal and maximal wavelength in order to avoid the effects of wind streaks in the turbulent boundary layer and the cut-off effect of SAR imaging of short sea surface waves. The values are set to $L_{min} = 30$ m and $L_{max} = 600$ m,

which corresponds to k_{max} = 0.2 and k_{min} = 0.01 in deep water.

Comparison of TerraSAR-X derived H_s with the significant wave height obtained by the buoy located at the Ekofisk oil platform in the North Sea (56°10'03"N, 3°32'32"E) shows a correlation of 0.83. TerraSAR-X derived peak wave length for National Data Buoy Center (NDBC) buoy 44066 (39°34'59"N, 72°36'2"W) and from the buoy located near the Ekofisk oil platform have a correlation of 0.95, an SI of 0.19 m, and an RMSE of 0.89 m, thus showing good agreement with in situ data. Comparison with NDBC buoys results in SI = 13% for peak wavelength measurement and SI = 21% for significant wave height.

Figure 4 shows wind and significant wave height fields estimated from a TerraSAR-X stripmap scene acquired over the Bay of Kiel in the Baltic Sea on December 10, 2012, and scatterplots for both algorithms. The number of entries is 371 for XMOD and 200 for XWAVE algorithms.

Remote-Sensing Data for Coastal Numerical Modeling

One area where spaceborne SAR systems have a significant impact is in the validation of wave forecast models. The forecast modeling services, for example, of the German Weather Service (DWD; http://www.dwd.de) are part of the global marine weather and warning system that provides wave forecasting in transocean shipping routes, storm prediction, and wave- and wind-related information for coastal protection and sport boats, all of which are important services for public safety. Third-generation wave models are now used for sea state prediction, including WAVEWATCH III used by NOAA and UKMET (United Kingdom Meteorological Office) and the WAM model used by European forecast services such as ECMWF, DWD, and the Danish Meteorological Institute (DMI, http://www.dmi.dk). The forecasts are also accessible to public users through Meteo France (MF, http://marine.meteofrance.com/marine).

In the open sea, these wave models are already capable of producing high-quality forecasts, as long as the wind
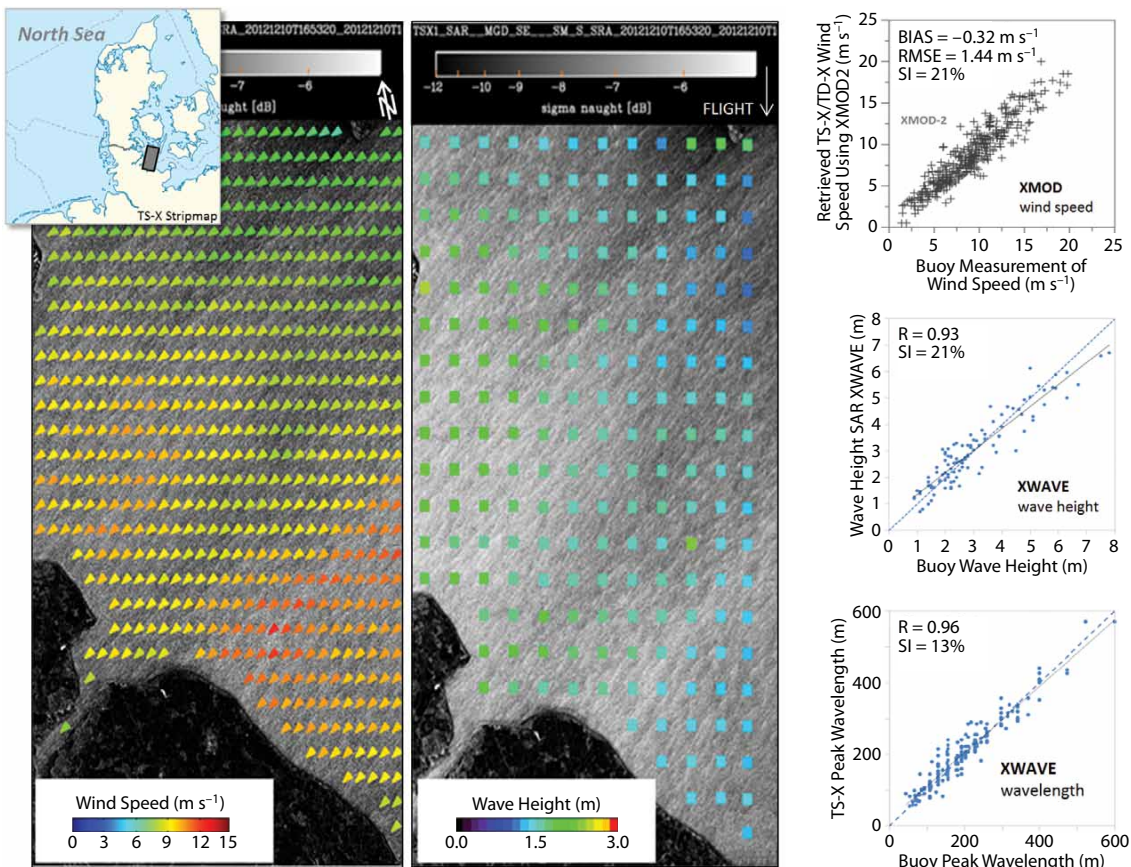

Figure 4. TerraSAR-X stripmap acquired over Kiel Bight in the Baltic Sea on December 10, 2012, at 16:53 UTC, and wind field derived using nonlinear XMOD-2 algorithms (left), significant wave height field derived using XWAVE-2 empirical algorithm (middle), and scatterplots for both algorithms (right). The number of entries is 371 for XMOD and 200 for XWAVE.

input from atmospheric forecast models and boundary conditions for sea state are correct. Uncertainties occur when dealing with numerical modeling and forecasting in coastal areas where physical processes in shallow water, caused by interactions among waves, currents, and the seafloor, become important. Wave properties can change greatly in coastal areas. Significant effort is required to include shallow water interactions in numerical schemes by coupling wave and circulation models through radiation stress and by tuning of the model functions and parameters for coastal processes like dissipation and wave breaking. Such coupled model forecast systems have been developed by several organizations (e.g., DWD,

Deltares, Helmholtz-Zentrum Geesthacht [GHZ]), and SAR data from high-resolution TerraSAR-X images have been particularly useful for validating these models.

In the course of an experimental investigation (Lehner et al., 2012), wind and sea state information retrieved from SAR were applied as input to a wave numerical spectral model (wind forcing and boundary condition) running at fine spatial horizontal resolution of 100 m. As boundary conditions, the wave spectra included swell obtained from the XWAVE algorithm and wind sea from JONSWAP spectra based on wind information derived using the XMOD algorithm from the same TerraSAR-X image. Results were compared to co-located

buoy measurements. Sensitivity tests for the German Bight in the North Sea (area around Helgoland Island and Hörnum Bight in the North Sea) were carried out for varying local wind speeds (with wind shadowing and gusts visible in TerraSAR-X images but not present in coarser wind data). The results showed sensitivity of local waves to wind variation and the importance of local wind effects on wave behavior. The varying retrieved TerraSAR-X wind speeds (increased and decreased by 3 m s^{-1} in Hörnum Bight) result in a large deviation of about ± 25% of modeled local wave height (Figure 5). Changing sea state properties strongly influence wave coupled processes: turbulent mixing in the water column and processes
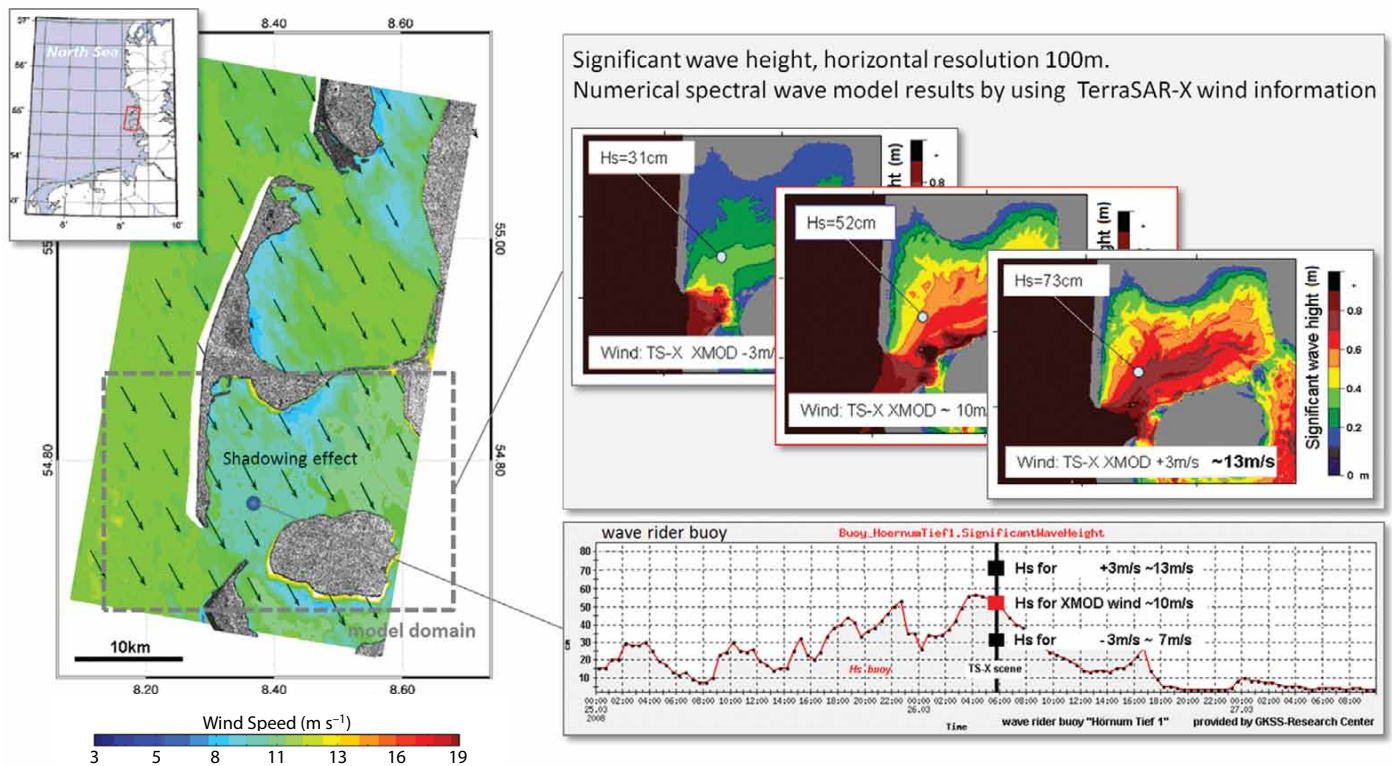

Figure 5. (left) Wind field retrieved using XMOD algorithm from a TerraSAR-X stripmap scene acquired over Sylt Island, North Sea, on March 26, 2008 (wind speed errors due to insufficient information are masked in white). (right) Sensitivity tests: wave height simulated by a numerical model on 100 m resolution mesh using TerraSAR-X derived wind speed (~ 10 m s^{-1}) at buoy position 54°46'2"N, 8°22'8"E corresponds well with buoy measurements (bottom right, in red). Varying the wind speed (increased and decreased at 3 m s^{-1}) results in strong deviations of about ~ 25% of wave height.

at the water-seabed boundary layer change significantly in shallow areas of the Wadden Sea.

Wave Breaking

Another process observed in TerraSAR-X imagery is wave breaking. Knowledge about the spatial distribution of wave heights along the shoreline, especially during storms, is an important issue and crucial for coastal protection. Furthermore, the predominant wave heights in the surf zone can prevent pirates from landing their boats along certain sections of the shore. Thus, information on surf height is of interest for protecting shipping lanes, preventing future attacks by pirates, and for coordinating international anti-piracy forces.

As a wave shoals, its height increases, leading to greater orbital velocity of water particles within the wave. Shoaling occurs until the wave's steepness exceeds a certain threshold, and it breaks. This occurs when orbital velocities in the wave exceed the wave's phase speed. When a wave breaks, water particles and bubbles fly into the air, and the water surface becomes very rough due to intense turbulence. All of this creates a strong echo in the radar signal. Smearing of the scatterers by Doppler shift due to high velocities results in streak-like structures at wave-breaking locations (Wackerman and Clemente-Colón, 2000). These signatures were investigated and their lengths used to estimate the radial speed of the scatterers, providing information about the propagation speed at the crest of the breaking wave and its possible amplitude before breaking (Brusch et al., 2011). Figure 6 shows a TerraSAR-X stripmap image acquired on November 21, 2008, at 17:00 UTC with incidence angle $\theta = 31°$. The white box at upper left highlights a small island located near Trischen Island in Elbe Estuary, and estimated mean breaking wave height adjacent to the island is indicated in red at bottom right.
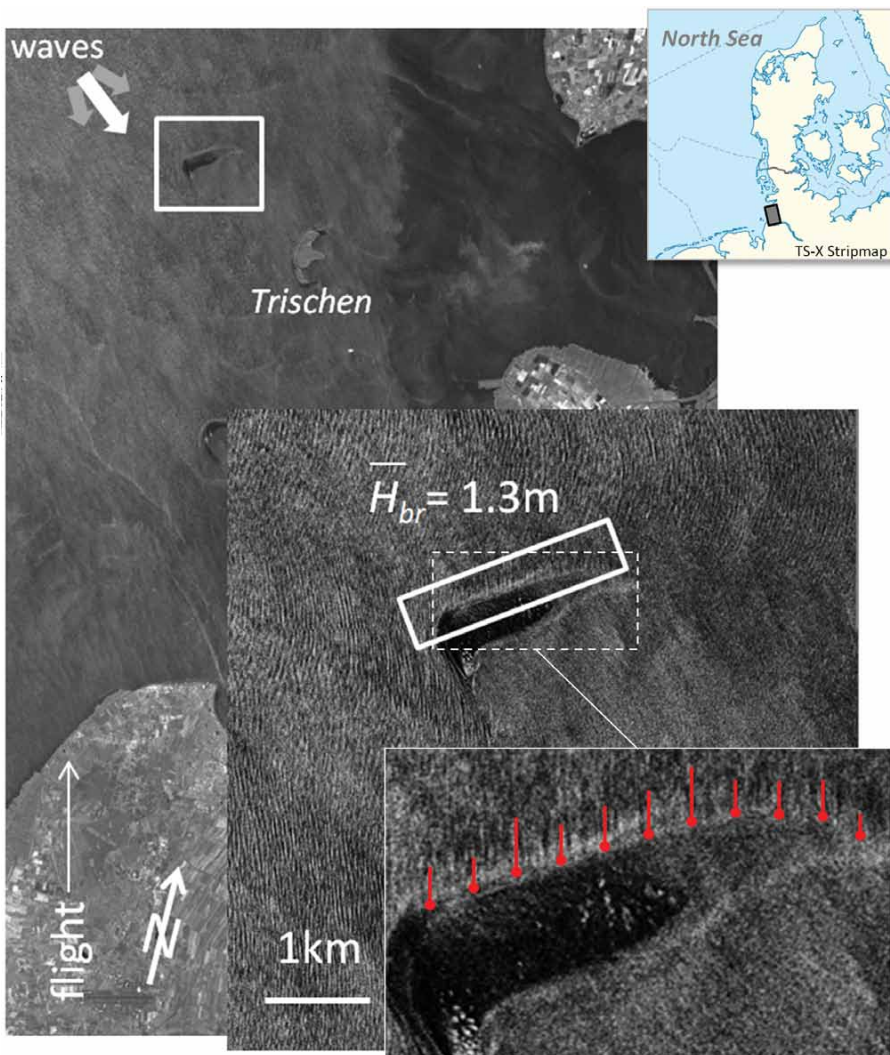
Wave Groups

Detection of wave groups in the ocean using TerraSAR-X data is among the first direct observations of such phenomena at high resolution. Wave groups were studied using data from earlier SAR missions by applying, for example, wavelet techniques (Niedermeier et al., 2005). Due to improved TerraSAR-X and TanDEM-X SAR properties, wave group parameters can be estimated directly using the XWAVE empirical algorithm.

Figure 7 shows an example of wave

Figure 6. TerraSAR-X stripmap image acquired on November 21, 2008, at 17:00 UTC with $\theta = 31°$. The white box at top left surrounds an island located near Trischen Island in Elbe Estuary. Breaking-wave signatures adjacent to the island are shown in red (bottom right). Estimated mean breaking wave height is $\bar{H}_{br} = 1.3$ m (1.6 for spilling breaking and 0.9 m for plunging breaking). The forecast significant wave height outside the bight is $H_s = 2.4$ m (DWD [German Weather Service] Global Spectral Model with 0.75° resolution) and 1.8 m using a nested model with 1 nm (1.8 km) resolution near the island.

groups observed near the Somalia coast. In the stripmap image acquired on November 18, 2010, at 14:56 UTC, the cross seas effect of two wave systems with about 1.8 m significant wave height is observed. Three wave groups are clearly visible; the wave height inside the groups is about 3 m. The origin of the wave groups in this location can be explained in different ways. The first possibility is local shoaling by underwater obstacles. According to the NOAA ETOPO 1-minute global relief, the local depth is about 2,000 m. This means that, in this case, local shoaling should be excluded from consideration. However, it is possible that a local flat-topped mountain exists there but was not imaged by NOAA's coarse data. The second possibility is the impact of local organized wind gusts. Moving convective cells in the atmosphere can produce a localized organized wind gust traveling with a speed close that of the swell system. Strong wind energy that feeds the same wave group for a longer time period can cause enormous growth of individual wave heights within the group (Rosenthal et al., 2011). The third explanation is a combination of phases of both wave systems, traveling with about a 50° phase difference from each other.

North Sea investigations show that abnormal height in wave groups is related to atmospheric effects. Pleskachevsky et al. (2012) found that such abnormal heights are caused by mesoscale wind gusts induced by open atmospheric cells that occur during cold air outbreaks and move across the sea as an organized system, "dragging" the growing waves. These results show local significant wave height increase on the order of meters within the cell, especially

in a narrow area of about 2.5 km at the footprint center of a cell. A group of cells under real storm conditions produces a local increase in significant wave height of more than 6 m during a short time window of 10 to 20 minutes (passing the cell). Wave groups, including extreme individual waves with wavelengths of more than 370 m beneath the cell's footprint, are estimated. This corresponds well with measurements of a rogue wave group with wavelengths of about 400 m recorded during the 2006 storm "Britta" that damaged the deck of research platform FiNO-1 located 18 m above mean sea level.

Ship Detection and Oil Spills

Scanning the ocean surface using remote-sensing instruments like SAR provides an opportunity not only to observe surrounding environmental processes but also to detect and monitor ships and turbulent ship wakes and waves (Lehner et al., 2013). With day and night coverage, weather independency, and global coverage, radar sensors onboard TerraSAR-X and its twin TanDEM-X are suitable for practical support of ship security and safety (Lehner et al., in press). Ship position, length, and speed can be identified, compared to Automatic Identification System
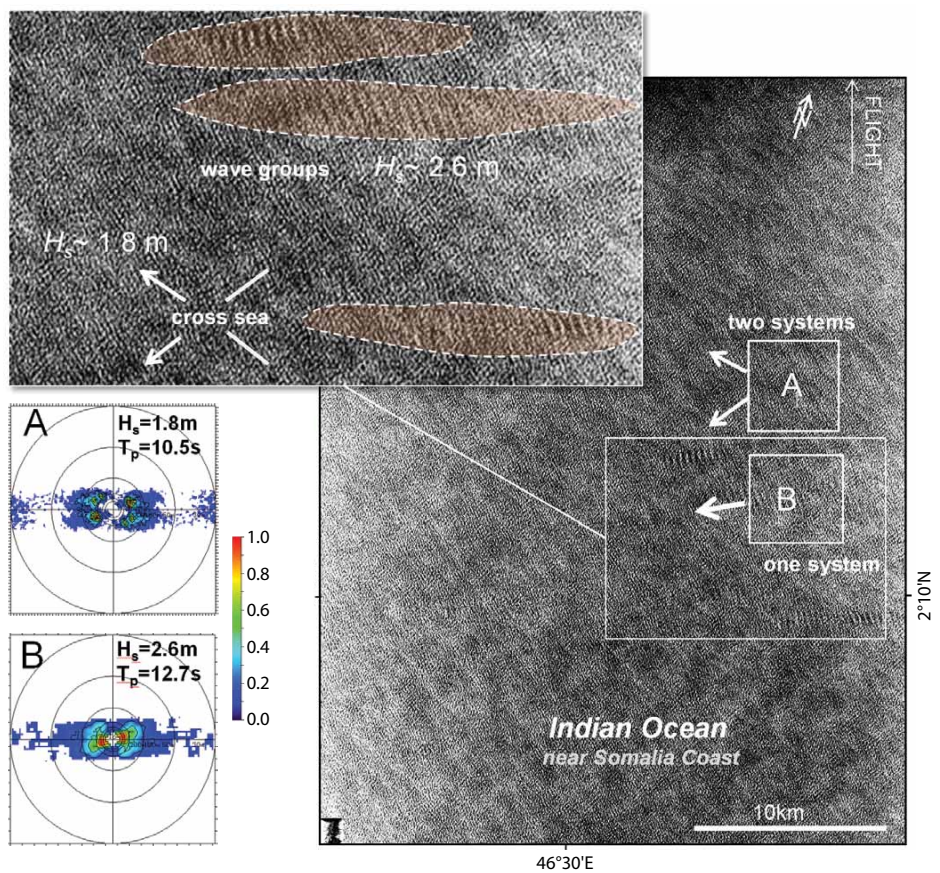

Figure 7. TerraSAR-X VV-polarized image acquired on November 18, 2010, at 14:56 UTC near the Somalia coast. For subscenes A (two-wave system observed) and B (a wave group), the spectra and estimated parameters are shown. According to National Oceanic and Atmospheric Administration 1 nm (1.8 km) bathymetry, the local depth is ~ 2,000 m.
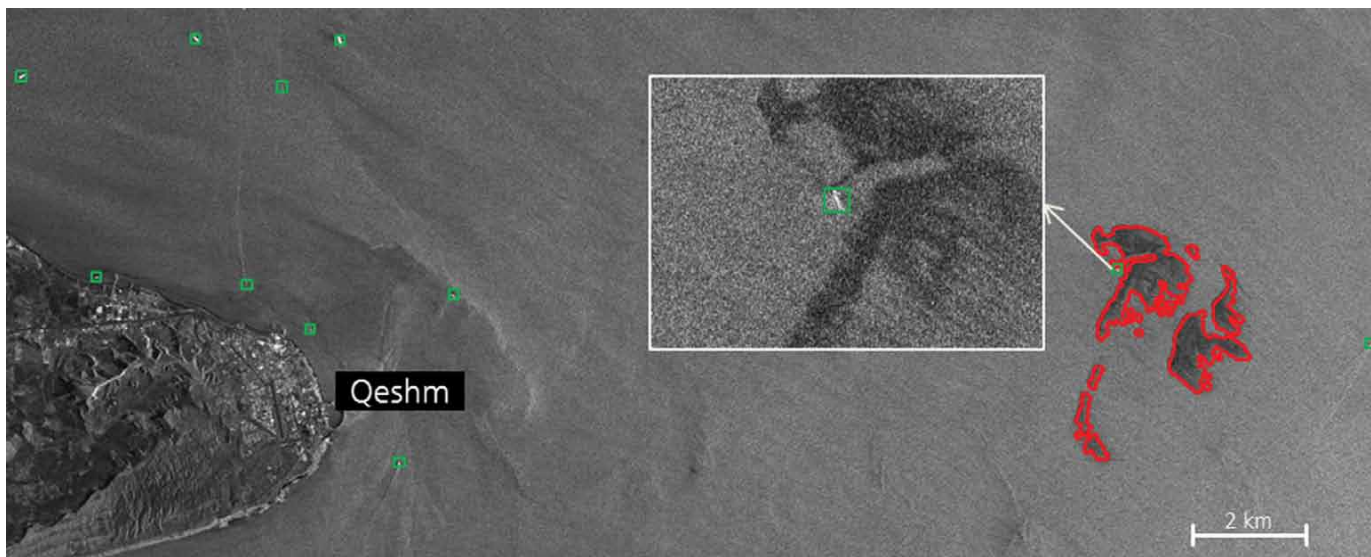
Figure 8. TerraSAR-X image acquired over the Strait of Hormuz, Iran, on July 24, 2009, at 02:22 UTC in stripmap mode, HH-polarization. This is a portion of the full image collected off the coast of Bandar Abbas, near Qeshm Island. Green rectangles show the results of ship detection using SAINT (© DLR), and the red outline was made using an oil spill detection algorithm. The white box is an enlargement of the polluted area showing the detected ship that was probably washing its tanks.

messages, and provided to integrated services. Instances of oil discharge from ships and platforms can also be detected (Velotto et al., 2011) and reported in near-real time. In addition to ship detection, surrounding marine and meteorological parameters can be estimated for operational oceanographic services (e.g., Schwarz et al., 2010).

The presence of surface slicks over the ocean surface attenuates short gravity-capillary waves. These waves, as well as long ocean waves, are the main sources of radar backscatter received by active microwave sensors. Reduction of the radar echo measured over a slick-covered area can be observed visually in an 8-bit scaled SAR image as a dark patch. However, detection of dark patches in SAR images of the ocean surface is only a preliminary step in the SAR oil spill detection algorithm; a detected dark region may not always be related to the presence of an oil spill because other oceanographic phenomena—such

as low wind areas, ship wakes, biogenic and natural slicks—have similar signatures (see Caruso et al., 2013, in this issue). Therefore, a classification procedure, based on probabilistic methods (i.e., Bayes classifier), machine learning techniques (i.e., Neural Network, Support Vector Machine), or a physical approach (either using amplitude image or polarimetric SAR data), is needed.

In addition, ships and man-made metallic objects present in the ocean environment (e.g., wind farms, platforms) call for all the three physical scattering models: (1) single-bounce returns caused by direct backscattering from surfaces perpendicular to the radar beam, (2) double-bounce returns due to the dihedral formed by a ship's vertical conducting plates and the sea surface, and (3) multiple-bounce returns caused by a ship's structural elements (e.g., deck and cables). Therefore, ships cause coherent scattering (i.e., measured NRCS by SAR) greater than that from the

surrounding sea surface. Figure 8 shows an example of combined oil and ship detection results obtained using high-resolution SAR data.

OUTLOOK

New high-resolution Earth observation data from SAR satellites allow estimation of ocean wave parameters and wind with high spatial resolution and quality. The SAR data can be used to validate spectral numerical wave models and to show and explain the interaction mechanisms among wind, waves, and seafloor. Analysis of TerraSAR-X images shows that it is possible to detect individual waves with wavelengths up to 30 m, their refraction, and wave shoaling. Underwater structures, such as banks, bars, and reefs, can be detected by long wave refraction. Wave energy flux can be estimated for purposes of protecting coastal equipment using SAR information. It is now possible to explore and obtain

underwater topography worldwide by remote-sensing data and by merging optical and SAR data. Although Envisat ASAR has not been available since 2012, its tasks will soon be assumed by a new mode of the TerraSAR-X satellite. The first page of this article shows the new ScanSAR Wide mode that covers an area 400 km × 250 km with 38 m resolution (standard ScanSAR covers about 100 km in the direction of flight with 18 m resolution). Although the image resolution is considerably lower than Envisat ASAR, the broad spatial coverage allows observation of processes such as tidal waves, atmospheric fronts, and wind gusts.

ACKNOWLEDGEMENTS

REFERENCES

Alpers, W.R., and C.L. Rufenach. 1979. The effect of orbital motions on synthetic aperture radar imagery of ocean waves. *IEEE Transactions on Antennas and Propagation* 27:685–690, http://dx.doi.org/10.1109/TAP.1979.1142163.

Breit, H., T. Fritz, U. Balss, M. Lachaise, A. Niedermeier, and M. Vonavka. 2010. TerraSAR-X SAR processing and products. *IEEE Transactions On Geoscience and Remote Sensing* 48:727–740, http://dx.doi.org/10.1109/TGRS.2009.2035497.

Bruck, M., M.T. Pontes, E. Azevedo, and S. Lehner. 2011. Study of sea-state variability and wave groupiness using TerraSAR-X synthetic aperture radar data. Pp. 1–7 in *Proceedings of the 9th EWTEC 2011*, 5–9 September 2011, Southampton, UK.

Bruck, M., and S. Lehner. 2010. Extraction of wave field from TerraSAR-X data. Paper presented at SEASAR 2010, Advances in SAR Oceanography from ENVISAT, ERS and ESA Third Party Missions, ESA ESRIN, Frascati/Rome, Italy, January 25–29, 2010.

Brusch, S., P. Held, S. Lehner, W. Rosenthal, and A. Pleskachevsky. 2011. Underwater bottom-topography in coastal areas from TerraSAR-X data. *International Journal of Remote Sensing* 32:4,527–4,543, http://dx.doi.org/10.1080/01431161.2010.489063.

Caruso, M.J., M. Migliaccio, J.T. Hargrove, O. Garcia-Pineda, and H.C. Graber. 2013. Oil spills and slicks imaged by synthetic aperture radar. *Oceanography* 26(2):112–123, http://dx.doi.org/10.5670/oceanog.2013.34.

Etling, D., and R.A. Brown. 1993. Roll vortices in the planetary boundary layer: A review. *Boundary-Layer Meteorology* 65:215–248, http://dx.doi.org/10.1007/BF00705527.

Lehner, S., A. Pleskachevsky, and M. Bruck. 2012. High resolution satellite measurements of coastal wind field and sea state. *International Journal of Remote Sensing* 33:7,337–7,360, http://dx.doi.org/10.1080/01431161.2012.685975.

Lehner, S., S. Brusch, and A. Pleskachevsky. 2013. Schiffsdetektion und Beobachtung des Kielwassers in hochaufgelösten TerraSAR-X Satellitenbildern und Sonarmessungen. Paper presented at a workshop held at the Maritime Technologie und Forschung, Forschungsbereich für Wasserschall und Geophysik (FWG).

Lehner, S., A. Pleskachevsky, S. Brusch, M. Bruck, M. Soccorsi, and D. Velotto. In press. Remote sensing of African waters using the high resolution TerraSAR-X satellite. In *Remote Sensing of the African Seas*. V. Barale and M. Gade, eds, Springer.

Li, X.-M., and S. Lehner. In press. Algorithm for sea surface wind retrieval from TerraSAR-X and TanDEM-X data. *IEEE Transactions on Geoscience and Remote Sensing*, http://dx.doi.org/10.1109/TGRS.2013.2267780.

Lyzenga, D.R., R.A. Shuchman, and J.D. Lyden. 1985. SAR imaging of waves in water and ice: Evidence for velocity bunching. *Journal of Geophysical Research* 90:1,031–1,036, http://dx.doi.org/10.1029/JC090iC01p01031.

Niedermeier, A., J.C. Nieto Borge, and S. Lehner. 2005. A wavelet-based algorithm to estimate ocean wave group parameters from radar images. *IEEE Transactions on Geoscience and Remote Sensing* 43:327–336, http://dx.doi.org/10.1109/TGRS.2004.836873.

Pontes, M., M. Bruck, S. Lehner, and A. Kabuth. 2010. Using satellite spectral wave data for wave energy resource characterization. Paper presented at the 3rd International Conference and Exhibition on Ocean Energy, October 6, 2010, Bilbao, Spain.

Pleskachevsky, A., S. Lehner, T. Heege, and C. Mott. 2011. Synergy and fusion of optical and synthetic aperture radar satellite data for underwater topography estimation in coastal areas. *Ocean Dynamics* 61:2,099–2,120, http://dx.doi.org/10.1007/s10236-011-0460-1.

Pleskachevsky, A., S. Lehner, and W. Rosenthal. 2012. Storm observations by remote sensing and influences of gustiness on ocean waves and on generation of rogue waves. *Ocean Dynamics* 62:1,335–1,351, http://dx.doi.org/10.1007/s10236-012-0567-z.

Ren, Y.-Z., S. Lehner, S. Brusch, X. Li, and M. He. 2012. An algorithm for the retrieval of sea surface wind fields using X-band TerraSAR-X data. *International Journal of Remote Sensing* 33:7,310–7,336, http://dx.doi.org/10.1080/01431161.2012.685977.

Rosenthal, W., A.L. Pleskachevsky, S. Lehner, and S. Brusch. 2011. Observation and modeling of high individual ocean waves and wave groups caused by a variable wind field. *Proceedings of the 12th International Workshop on Wave Hindcasting and Forecasting*, October 30–November 4, 2011, Kohala Coast, Big Island, Hawaii. Available online at: http://jcomm.info/images/stories/2011/12thWaves/Papers/2011_workshop-wavehind-and-forecasting__rosenthal_pleskachevsky_lehner_brusch.pdf (accessed September 20, 2013).

Schwarz, E., S. Lehner, and S. Brusch. 2010. Ship detection service. Pp. 115–118 in *Proceedings of the Geoforum MV 2010 Vernetzte Geodaten: Vom Sensor zum WEB*, April 26–27, 2010, Rostock-Warnemünde.

Sikora, T., and S. Ufermann. 2000. Marine atmospheric boundary layer. Cellular convection and longitudinal roll vortices. Pp. 321–330 (Chapter 14) in *Synthetic Aperture Radar Marine User's Manual*. C.R. Jackson and J.R. Apel, eds, NOAA NESDIS Office of Research and Applications, Washington, DC. Available online at: http://www.sarusersmanual.com (accessed September 20, 2013).

Velotto, D., M. Migliaccio, F. Nunziata, and S. Lehner, 2011. Dual-polarized TerraSAR-X data for oil-spill observation. *IEEE Transactions on Geoscience and Remote Sensing* 49:4,751–4,762, http://dx.doi.org/10.1109/TGRS.2011.2162960.

Wackerman, C.W., and P. Clemente-Colón. 2000. Wave refraction, breaking and other near-shore processes. Pp. 171–189 (Chapter 6) in *Synthetic Aperture Radar Marine User's Manual*. C.R. Jackson and J.R. Apel, eds, NOAA NESDIS Office of Research and Applications, Washington, DC. Available online at: http://www.sarusersmanual.com (accessed September 20, 2013).